J|A|C|S
ARTICLES

Published on Web 09/14/2010

Unstitching the Nanoscopic Mystery of Zeolite Crystal Formation

Rhea Brent,[†] Pablo Cubillas,[†] Sam M. Stevens,[†,‡] Kim E. Jelfs,[§] Ayako Umemura,[†] James T. Gebbie,[†] Ben Slater,[§] Osamu Terasaki,[‡,||] Mark A. Holden,[†] and Michael W. Anderson*[,†]

Centre for Nanoporous Materials, School of Chemistry, The University of Manchester, Oxford Road, Manchester M13 9PL, U.K., Department of Physical, Inorganic and Structural Chemistry, Stockholm University, 10691 Stockholm, Sweden, Department of Chemistry, University College London, 20 Gordon Street, London WC1H 0AJ, U.K., and Graduate School of EEWS (WCU), KAIST, Taejon 305-701, Korea

Received July 9, 2010; E-mail: m.anderson@manchester.ac.uk

Abstract: A molecular-scale understanding of crystal growth is critical to the development of important materials such as pharmaceuticals, semiconductors and catalysts. Only recently has this been possible with the advent of atomic force microscopy that permits observation of nanoscopic features on solid surfaces under a liquid or solution environment. This allows *in situ* measurement of important chemical transformations such as crystal growth and dissolution. Further, the microscope can access not only an accurate height measurement of surface topography, important to deduce structural elements, but also the forces involved during nanoscopic processes. We have discovered that it is possible to use these features to "illuminate" critical nanoscopic chemical events at crystal surfaces and at the same time extract the associated energies and unstitch the details of the stepwise mechanism of growth and dissolution. This approach has been developed using nanoporous crystals of the heterogeneous catalyst zeolite L; however, in principle the approach could be adapted to many crystal growth problems.

1. Introduction

The crux of crystal growth is to understand the axioms, the fundamental rules by which crystals become organized. These rules are unlikely to be subtle and indistinct as this will lead to indiscriminate and amorphous growth. It is more likely that such rules are definite and the associated energies distinct enough to yield crystals of determinate form. Complications, such as intergrowths and defects, will be incorporated when competitive yet distinct rules are in play. The process of crystal growth has often been envisaged as a succession of fundamental nanoscale events occurring according to a set of probabilities, the rate constants associated with the activation energies of these processes.[1−5] Nucleation on low index faces, the stable surfaces, e.g. (100), is an unfavorable event with associated slow kinetics. Rough surfaces festooned with kink sites, such as the (111) facet of a cubic crystal, expose sites for favorable growth.[6] Crystals that exhibit a high screw-dislocation density provide perpetual spiral growth fronts permitting favorable growth on low index faces even at low supersaturation. In principle these are the axioms of crystal growth viewed at the nanoscale. However, crystals are many and varied and, as a consequence, the variety in the specifics of the rules will naturally be extensive. Moreover, until the advent of scanning probe microscopies[7] it has not been possible to observe directly these fundamental processes and thereby properly test these overall conjectures[1] let alone the details of individual test cases. Here we apply a combination of *in situ* atomic force microscopy (AFM),[8] high-resolution scanning electron microscopy (HRSEM)[9] and theoretical modeling to understand nanoscale processes during the dissolution and growth of zeolite L. Through careful operation of the AFM it is possible to highlight exactly where the crystal chemistry takes place and then probe every step in the dissolution process. Then through Monte Carlo simulation of crystal surfaces it is possible to model the growth process. This permits not only a study of the mechanism of growth and dissolution under real conditions but also measurement of activation barriers to fundamental molecular events and associated enthalpies.

Zeolite L is a framework aluminosilicate with one-dimensional pores of subnanometer diameter[10] that is used, for

[†] The University of Manchester.
[‡] Stockholm University.
[§] University College London.
[||] KAIST.

(1) Burton, W. K.; Cabrera, N.; Frank, F. C. *Philos. Trans. R. Soc., A* **1951**, *243*, 299–358.
(2) Hartman, P.; Perdok, W. G. *Acta Crystallogr.* **1955**, *8*, 49–52.
(3) Hartman, P.; Perdok, W. G. *Acta Crystallogr.* **1955**, *8*, 521–524.
(4) Hartman, P.; Perdok, W. G. *Acta Crystallogr.* **1955**, *8*, 525–529.
(5) Roberts, K. J.; Docherty, R.; Bennema, P.; Jetten, L. A. M. J. *J. Phys. D: Appl. Phys.* **1993**, *26*, B7–B21.
(6) Cabrera, N.; Burton, W. K. *Discuss. Faraday Soc.* **1949**, *5*, 40–48.
(7) Binnig, G.; Rohrer, H.; Gerber, C.; Weibel, E. *Phys. Rev. Lett.* **1982**, *49*, 57–61. Binnig, G.; Quate, C. F.; Gerber, C. *Phys. Rev. Lett.* **1986**, *56*, 930–933.
(8) Meza, L. I.; Anderson, M. W.; Agger, J. R. *Chem. Commun.* **2007**, 2473–2475.
(9) Stevens, S. M.; Cubillas, P.; Jansson, K.; Terasaki, O.; Anderson, M. W.; Wright, P. A.; Castro, M. *Chem. Commun.* **2008**, 3894–3896.
(10) Barrer, R. M.; Villiger, H. *Z. Kristallogr.* **1969**, *128*, 352–370.

 10.1021/ja105593v

instance, in the catalytic dehydrocyclization of light naphtha in the presence of Pt metal.[11] Typical crystallizations from aqueous solution result in long hexagonal prisms with the unidimensional pores running along the long axis of the crystal.[10] In applications that require guest species to diffuse into and out of the pore system there is a distinct advantage to reduce the path length of the pores by shortening the long axis of the crystal. This can be achieved either by changing crystallization conditions or by adding habit modifiers to the preparation.[12] A nanoscopic understanding of the crystal growth processes could be used to engineer materials with reduced path lengths.

2. Experimental Section

2.1. Synthesis of Zeolite L. Crystals of zeolite L were synthesized according to the method outlined elsewhere,[13] with a molar gel composition of 10.2 K_2O:1 Al_2O_3:20 SiO_2:1030 H_2O. The gel was heated in an autoclave at 180 °C for 3 days. After crystallization the autoclave was quenched in order to prevent surface restructuring during cooling. The crystals obtained were long hexagonal cylinders with average dimensions of 3.8 × 1.5 μm, determined by scanning electron microscopy (FEI Quanta ESEM).

2.2. AFM Protocol. *In situ* AFM was carried out using a JPK NanoWizard II equipped with a temperature-controllable Biocell for imaging under liquids. All experiments were carried out in contact mode using silicon nitride V-shaped cantilevers with a nominal force constant of 0.58 N m^{-1} (supplied by Veeco Probes NP). Crystals were fixed in place by dispersing over a resin and curing at 60 °C. 300 μL of sodium hydroxide (0.2 M) was injected onto the sample, and the imaging was carried out under static conditions. The image size was approximately 2.5 × 0.7 μm with a scan rate of 2.5 Hz. Two types of AFM experiments were carried out: (1) continuous scanning, where the slow scan axis was enabled; (2) line scanning, where only a single line was scanned by disabling the slow scan axis.

The load exerted by the AFM tip was calculated according to

$$F_N = K_N S_N V_N \quad (1)$$

where K_N = vertical spring constant (N m^{-1}); S_N = vertical sensitivity (m V^{-1}); V_N = set point (V). The vertical sensitivity (S_N) was calculated from the slope of a force−distance curve taken during the experiment. The vertical spring constant (K_N) was measured using the thermal vibration method.[14] In order to ensure a constant load during the duration of the experiments force−distance curves were acquired every few scans and the set point adjusted accordingly. No significant change in load (>5 nN) was ever observed. Continuous scanning experiments were carried out at loads varying between 4.9 and 35.6 nN at two different temperatures, 298 and 313 K. The dissolution rate was determined for each load at the two different temperatures.

2.3. High-Resolution Scanning Electron Microscopy. High-resolution scanning electron micrographs were collected using a JEOL JSM-7401F fitted with a cold field emission gun (FEG) on uncoated samples. As the zeolite is electrically insulating, in order to observe surface fine structure it is necessary to use low impact energy electrons. At the same time, in order to optimize resolution the accelerating voltage and sample-stage bias are set to 2.3 kV and 1.5 kV, respectively, which results in an impact energy of 800 eV (so-called gentle beam). Crystals were affixed to a polished, high-density graphite rod to aid conduction. Samples were heated to 250 °C before insertion into the SEM chamber to reduce contamination and allowed to cool to prevent thermal drift. Electrons were detected using an in-lens detector with a working distance of 1.5 mm to improve the signal-to-noise.

2.4. Simulations. Simulations to calculate activation barriers to dissolution of silicate and aluminosilicate dimers in an aqueous environment were performed using the DFT code CP2K.[15] The PBE functional[16] was applied with molecularly optimized double-zeta valence polarized basis sets.[17] The transition states were obtained using the "dimer" mode-following method.[18] The clusters were microsolvated with eight water molecules to include solvation effects. Molecular dynamics (MD) simulations using an NVE ensemble were carried out at 300 K for 1 ps followed by 150 K for 1 ps to anneal the starting configurations. The stepwise dissolution simulation was achieved using an approach more fully described elsewhere.[19,20] Monte Carlo simulations were performed using an in-house C++ program with graphics simulated in OpenGL.

3. Results and Discussion

Figure 1 shows a series of *in situ* AFM measurements recorded on a $\{10\bar{1}0\}$ facet during the dissolution of zeolite L under a 0.2 M solution of sodium hydroxide. The images are recorded in lateral deflection mode which monitors the twisting of the AFM cantilever, a mode normally used in nanotribology studies to measure local, atomic scale, frictional forces. Immediately evident from these images are the bright areas predominantly at the ends of the long narrow terraces. We have previously established[21] that these long narrow terraces are chains of cancrinite cages (see Figure 2) where, in the limit, the terrace is an individual cancrinite cage column. Subsequent images show that the area corresponding to the bright region in the previous image is absent indicating clearly that the bright region on the crystal is the part that is dissolving. Closer examination shows that the terraces of zeolite L have long straight edges with intermittent shoulders (see high-resolution scanning electron micrograph (HRSEM) and AFM in Figure 3). The shoulders, that are a consequence of the fusion of two terraces, contain a high density of kink sites that are exposed as bright areas in the lateral deflection images (circled in Figure 1vi). This shows how vividly the dissolving regions of the crystal are targeted by monitoring lateral deflection compared with the corresponding vertical deflection AFM image (shown in Figure 1i). Where the chemistry is taking place energy is imparted into the cantilever which results in a readily measurable lateral deflection response. We find that this phenomenon is generally observed during both growth and dissolution experiments on a variety of crystal systems and is further illustrated for growth of the nanoporous sodalite zincophosphate (see Supporting Information).

3.1. Rates from AFM. Considering the bright areas in the lateral deflection AFM image in Figure 1 it is apparent that, as the tip scans from top to bottom, the top of the cancrinite column is dissolved more than the bottom of the cancrinite column and *vice versa*. This illustrates two things: first, the tip is aiding the

(11) Bernard, J. R. *Proc. 5th Int. Zeolite Conf., Napoli*; Rees, L. V. C., Ed.; Heyden: London, 1980; p 686.
(12) Larlus, O.; Valtchev, V. P. *Chem. Mater.* **2004**, *16*, 3381–3389.
(13) Lee, Y.-J.; Lee, J. S.; Yoon, K. B. *Microporous Mesoporous Mater.* **2005**, *80*, 237–246.
(14) Hutter, J. L.; Bechhoefer, J. *Rev. Sci. Instrum.* **1993**, *64*, 1868–1873.
(15) VandeVondele, J.; Krack, M.; Mohamed, F.; Parrinello, M.; Chasaing, T.; Hutter, J. *Comput. Phys. Commun.* **2005**, *167*, 103–128.
(16) Perdew, J. P.; Burke, K.; Ernzerhof, M. *Phys. Rev. Lett.* **1996**, *77*, 3865–3868.
(17) VandeVondele, J.; Hutter, J. *J. Chem. Phys.* **2007**, *127*, 114105.
(18) Henkelman, G.; Jonsson, H. *J. Chem. Phys.* **1999**, *111*, 7010–7022.
(19) Chiu, M. E.; Slater, B.; Gale, J. D. *Angew. Chem., Int. Ed.* **2005**, *44*, 1213–1217.
(20) Meza, L. I.; Anderson, M. W.; Slater, B.; Agger, J. R. *Phys. Chem. Chem. Phys.* **2008**, *10*, 5066–5076.
(21) Brent, R.; Anderson, M. W. *Angew. Chem., Int. Ed.* **2008**, *29*, 5327–5330.

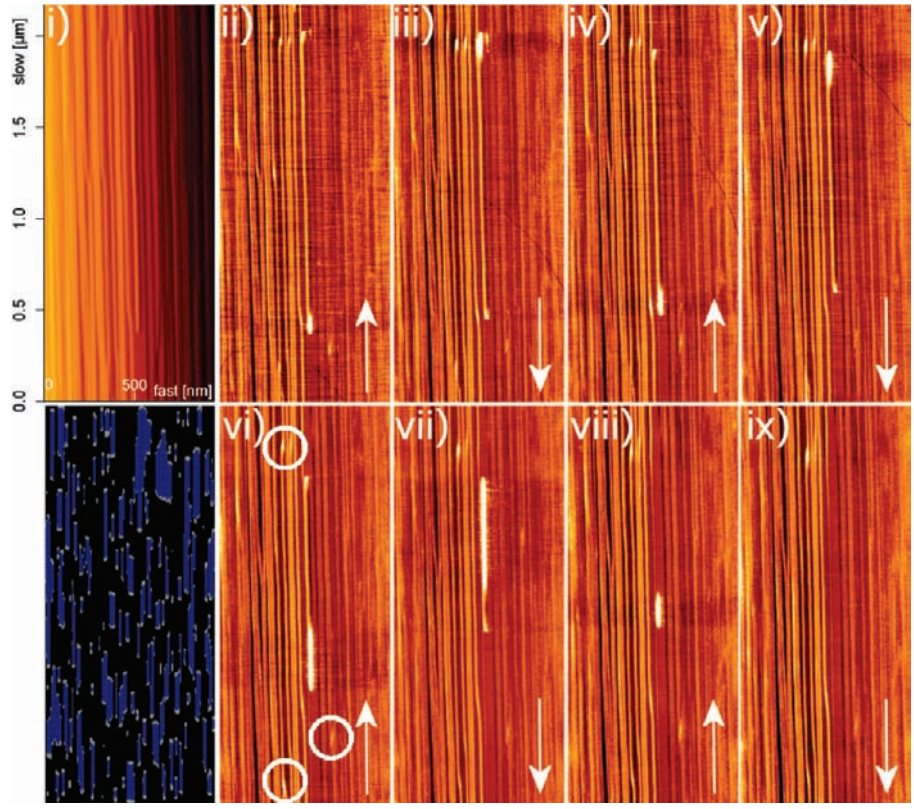

Figure 1. Atomic force micrographs of a $\{10\bar{1}0\}$ face of zeolite L during dissolution in 0.2 M NaOH. The image in (i) shows a vertical deflection micrograph at the beginning of the experiment, and (ii−ix) show lateral deflection micrographs on subsequent scans over the crystal surface. The time between each image was approximately four minutes. The bright white areas indicate a change in friction experienced by the AFM tip, shown as a high contrast change on the image. The white arrows indicate the direction of movement of the slow scan axis. The white circles in image (vi) highlight the bright contrast associated with kink site dissolution. Image in lower left shows Monte Carlo calculation for dissolution in undersaturated conditions at 40 °C using the same energy scale (Figure 8) for crystal growth and a stabilization of bidentate attachment, U_B, of 4 kcal mol^{-1}. Dissolution sites highlighted in white indicate preferential dissolution at cancrinite column ends and at terrace kink sites.

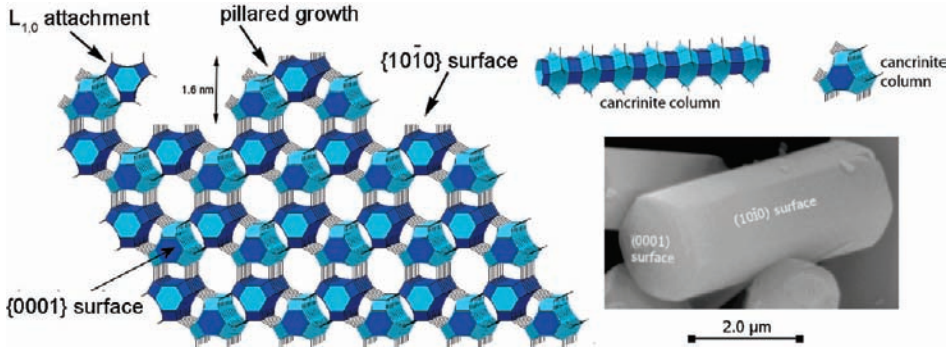

Figure 2. Schematic diagram showing the connectivity of zeolite L. A $\{10\bar{1}0\}$ face is composed of long cancrinite columns. In order to form the porous structure on this facet, the cancrinite columns must form a bridge between two adjacent pillars. This can be achieved either by pillared growth where two pillars are laid down and then capped or by the rather unfavorable side attachment *via* an $L_{1,0}$ bidentate linkage (see Figure 8). This latter scenario is less likely to stick and complete the terrace except at high supersaturation. The scanning electron micrograph shows the morphology of zeolite L crystals used in this study. The $\{10\bar{1}0\}$ facet is verified as such owing to the height of surface features consistent with these planes and inconsistent with a $\{1\bar{2}10\}$ plane that would have been another possibility.

crystal dissolution; second, the length of the bright region is related to the relative rate of the tip movement and the terrace-end movement. When these are in the same direction, a long bright area ensues, and when they are opposed a short bright area ensues. As the tip velocity is known it is possible to accurately determine the terrace-retreat velocity.

The rate was calculated by utilizing the observation of a high degree of contrast change ("bright regions") for the dissolving part of the terrace, at a particular time on the lateral deflection images. Because the bright regions highlight the dissolving part of the crystal, a relationship relating the length of the bright regions to the dissolution rate could be derived; this is shown in Figure 4a and eq 2. AFM images showing how y was measured are shown in Figure 4b.

$$\text{as} \qquad v_{\text{tip}} = \frac{(r_t + y)}{t}$$

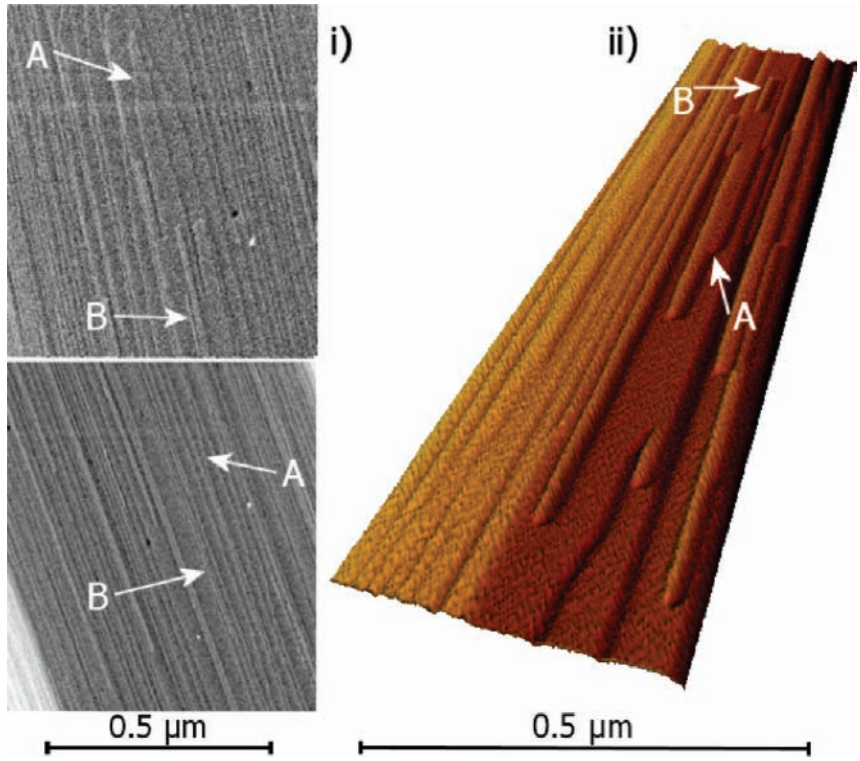

Figure 3. Comparison of HRSEM and AFM micrographs. Micrographs showing the straight narrow cancrinite columns (noted as B by arrows) and shoulders (noted as A by arrows) present on a $\{10\bar{1}0\}$ face of zeolite L. The images in (i) are high-resolution scanning electron micrographs, and (ii) is a 3-D representation of an atomic force micrograph.

$$\text{and} \qquad v_t = \frac{y}{t}$$

$$\therefore \frac{v_{tip}}{v_t} = \frac{(r_t + y)}{y} \qquad \text{or} \qquad \therefore \frac{v_{tip}}{v_t} = \frac{(r_t - y')}{y'}$$

$$\therefore v_t = \frac{y}{(r_t + y)} v_{tip} \propto \frac{y}{(r_t + y)} \qquad \text{or}$$

$$\therefore v_t = \frac{y'}{(r_t - y)} v_{tip} \propto \frac{y'}{(r_t - y')} \quad (2)$$

where y or $y' =$ length of the bright spot that has dissolved (nm); $t =$ time the tip is in contact with the terrace (s); $v_{tip} =$ velocity of the tip (nm s^{-1}); $v_t =$ velocity of tip aided dissolution (nm s^{-1}); $r_t =$ tip radius (nm).

The tip radius was determined by imaging the sample of interest, zeolite L. The 1.6 nm features on its surface are ideal for reverse imaging of the tip shape in the lateral dimension. From this, it was assumed that the tip has a spherical shape and therefore the dimension perpendicular to the scan direction would be equal to that obtained in the lateral dimension. It was more appropriate to use the equation involving y, as opposed to y', since y' was often small and therefore difficult to measure accurately.

3.2. Effect of Load on Dissolution Rate. Combined chemical and mechanical attack using AFM in chemically corrosive conditions is often effective for material removal and has been applied in a wide variety of contexts.[22−26] One example is the dissolution of calcite, which has been extensively studied by AFM. Dickinson et al.[27] demonstrated corrosive wear by continuously scanning the AFM tip back and forth over an etch pit at high force (160 nN). They found that the etch pit increased along the line of the tip scan direction, while remaining unchanged in the unscanned areas of the terrace. This showed the synergistic effect of the corrosive environment and the mechanical loading on the wear of the material.

For the case of zeolite L it was observed that as the AFM tip load increases so does the dissolution rate. This is shown in Figure 5. It can be seen that there are two distinct regions on the graph, for a given temperature, dependent upon the applied load. In the first region, below 20 nN, the dissolution is not linear. When the load approaches 20 nN, a sudden increase in dissolution rate is observed, followed by a linear increase. Above 20 nN the linear plots at the two temperatures are identical. The two-phase dissolution rate versus load plot suggests that there is a change in the process by which the terrace dissolves. As the load is increased, the pressure exerted will also increase until a point at which pressure-induced amorphization (PIA) may occur. For zeolite A, calculations suggest that the pressure required to obtain a low-density amorphous phase (LDA) is approximately 2 GPa.[28]

The maximum radial stress adjacent to the AFM tip can be estimated using eq 3.[29] The effects of stress are generally greatly

(22) Gnecco, E.; Bennewitz, R.; Meyer, E. *Phys. Rev. Lett.* **2002**, *88*, 215501.
(23) Park, N.-S.; Kim, M.-W.; Langford, S. C.; Dickinson, J. T. *J. Appl. Phys.* **1996**, *80*, 2680–2686.
(24) Kopta, S.; Salmeron, M. *J. Chem. Phys.* **2000**, *113*, 8249–8252.
(25) Gotsmann, B.; Durig, U. *Langmuir* **2004**, *20*, 1495–1500.
(26) Jiang, Z. G.; Lu, C. J.; Bogy, D. B.; Bhatia, C. S.; Miyamoto, T. *Thin Solid Films* **1995**, *258*, 75–81.
(27) Dickinson, J. T.; Scudiero, L.; Yasuda, K.; Kim, M. W.; Langford, S. C. *Tribol. Lett.* **1997**, *3*, 53–67.
(28) Peral, I.; Iñiguez, J. *Phys. Rev. Lett.* **2006**, *97*, 225502.

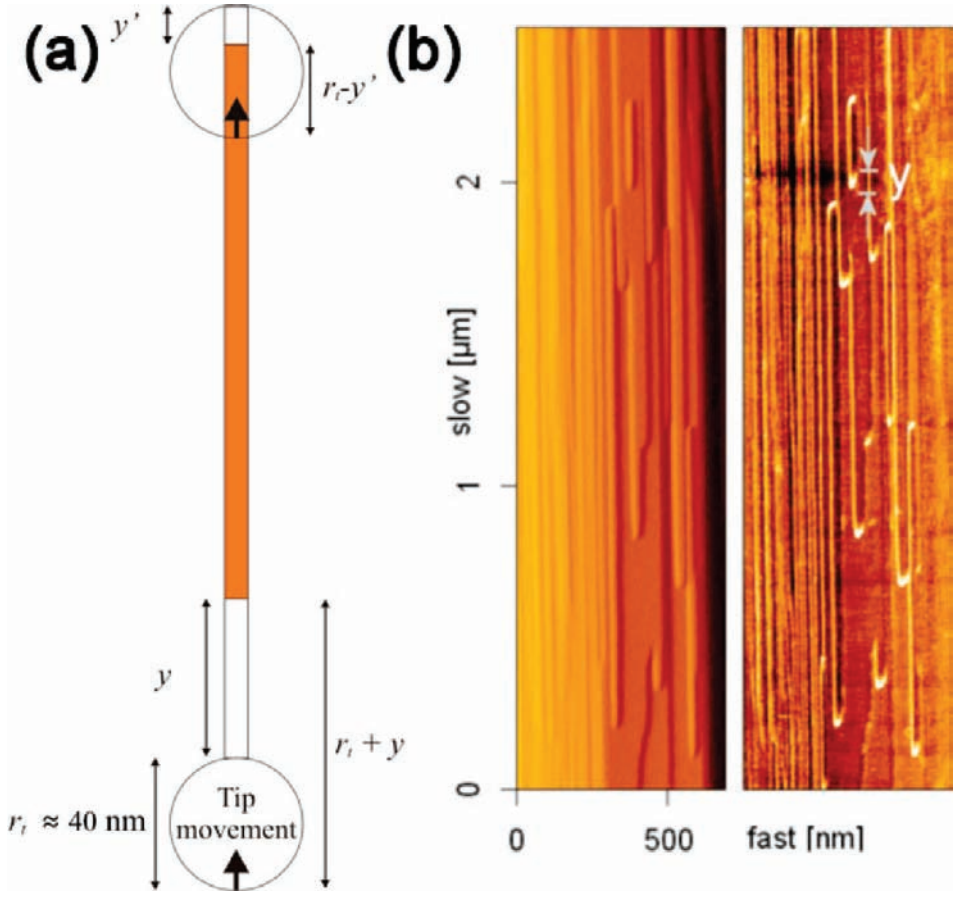

Figure 4. (a) Schematic of the dissolution of 1.6 nm terrace of zeolite L, where the white part is the dissolving part of the terrace and the orange part is the nondissolving part of the terrace. The circle represents the contact area of the tip. (b) Atomic force micrographs of the vertical and lateral deflections of zeolite L {10$\bar{1}$0}. The right-hand image shows the lateral deflection, where the arrows showing *y* correspond to the distance measured to determine dissolution rates.

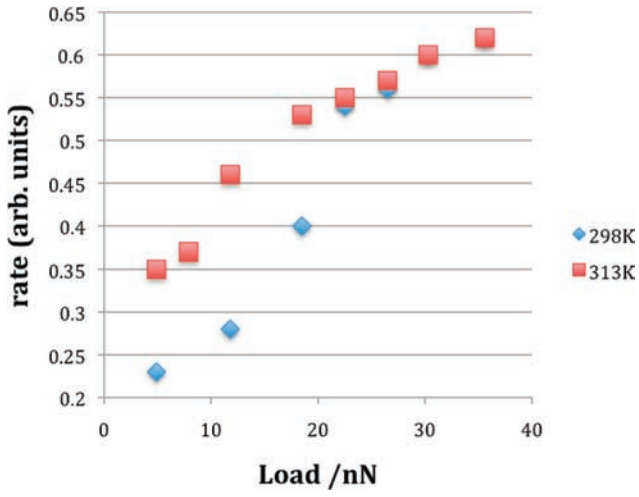

Figure 5. Plot of zeolite L dissolution rate versus AFM tip load at two solution temperatures in a 0.2 M solution of NaOH.

enhanced when the tip moves over terraces because the connectivity of units to the bulk is lower.

$$\sigma_r = \frac{1-2\nu}{\pi}\left[\frac{2F_N E^2}{9(1-\nu^2)^2 r_t^2}\right]^{1/3} \quad (3)$$

where E = Young's modulus of sample (Pa); ν = Poisson's ratio of sample; F_N = applied normal force (N); r_t = tip radius of curvature (m); σ_r = maximum radial stress (Pa).

Table 1. Calculated Maximum Radial Stress at Various Applied Loads

load/nN	maximum radial stress/GPa
4.9	1.23
11.8	1.64
18.5	1.91
22.5	2.03
26.5	2.15
30.3	2.24
35.6	2.36

The maximum calculated radial stress exerted on zeolite L for each applied normal load (at 298 K) is shown in Table 1. Since the values of E and ν for the sample zeolite L are not known, those of a closely related mineral were used. Microcline is a potassium aluminum silicate which belongs to the feldspar group of minerals. It has a Young's modulus of 7.1×10^{10} Pa and Poisson's ratio of ~0.16.[30] It can be seen that, for loads above 20 nN, the calculated pressure was higher than 2 GPa, i.e. above the critical point calculated to induce PIA for zeolite A.[28]

The enhancement in the dissolution through this tip-aided process can then be viewed in two complementary ways. First, the applied stress from the cantilever lowers the activation

(29) Timoshenko, S. P.; Goodier, J. N. *Theory of Elasticity*; McGraw-Hill: New York, 1987.
(30) Zaslavskii, B. I.; Krupnyi, A. I.; Aleksandrov, K. S. *Izv. Akad. Nauk SSSR, Fiz. Zemli* **1974**, 55.

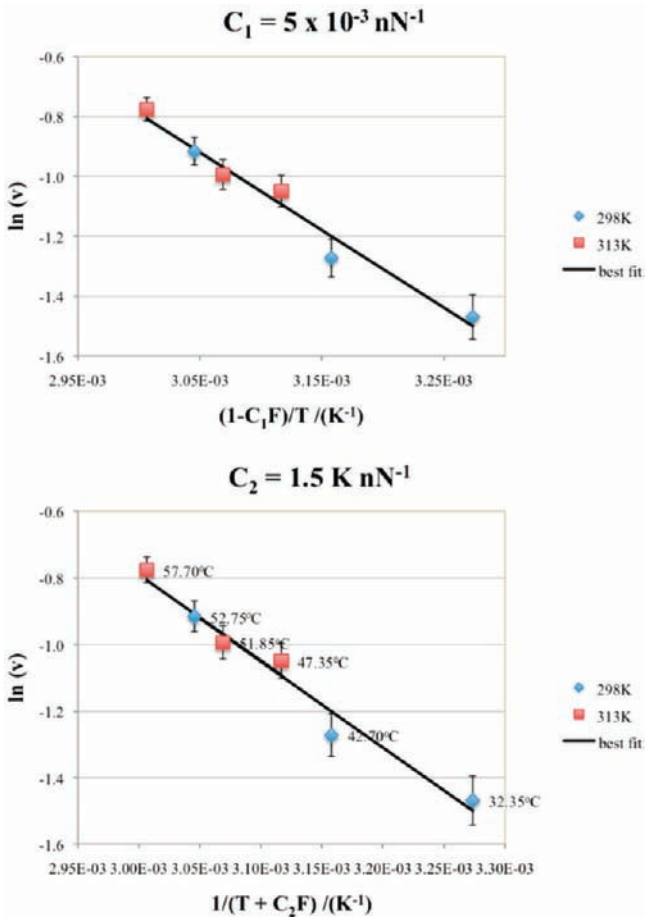

Figure 6. Arrhenius plots for dissolution of zeolite L in 0.2 M NaOH solution at two solution temperatures: 298 K; 313 K. The lower plot is based on a local heating of the zeolite surface and indicates nominal temperature. The upper plot is based on a decrease in the activation energy caused by local deformation. The constants C_1 and C_2 were determined by minimization of the root-mean-square deviation between the experimental data and a line of best fit.

energy for bond breaking in a similar manner to that discussed previously for mica.[31] The apparent activation energy, E_a, reduces to $E_a - \delta E_a$, where δE_a is proportional to the applied normal load, F_N, with a constant of proportionality C_1. In this case an appropriate Arrhenius expression for dissolution becomes

$$\ln(\text{rate}) = \frac{-E_a(1 - C_1F_N)}{RT} \quad (4)$$

A second way to envisage the problem is that the applied load results in a local heating which again is proportional to the normal load with a constant of proportionality C_2. In this case the Arrhenius expression becomes:

$$\ln(\text{rate}) = \frac{-E_a}{R(T + C_2F_N)} \quad (5)$$

The two approaches are more or less equivalent, and Arrhenius plots yield very similar activation energies (see Figure 6): $E_a = 21.5$ kJ mol^{-1} in the case of a lowered activation energy; $E_a = 23.1$ kJ mol^{-1} for a local temperature elevation. The second approach gives a nominal increase in temperature by *ca.* 1.5 °C/nN. This Arrhenius behavior is linear until a critical pressure, *ca.* 2 GPa, is reached and the structure undergoes a more substantial pressure induced amorphization. Assuming that the formation of an activated complex involving five-coordinate silicon through attack by an OH− group will be rate-determining (we find attack at aluminum to be more favorable by over 30 kJ mol^{-1}), the best theoretical estimate is ∼35−45 kJ mol^{-1},[32,33] similar to the measured value obtained here and the experimental value of 27.4 kJ mol^{-1} reported for the dissolution of the mineral heulandite.[34] Measurements of the rate of dissolution made under different pH conditions show that the order of the dissolution process is 0.31 with respect to OH$^-$,[35] which is in close agreement with bulk measurements made on related mineral phases.[36]

In order to probe the finer details of the dissolution process it is possible to harness the principle of tip-aided dissolution. The tip was rastered continuously across the same scan line, across the middle of a 1.6 nm high terrace consisting of three bridged cancrinite columns (see Figure 2), at a rate of 2.5 Hz permitting very rapid measurement of dissolution events. These events could be uniquely classified according to the lateral deflection response of the cantilever that may be converted into an equivalent energy dissipation.[35] Figure 7 shows how the continuous line scan eventually cuts through a terrace, but this occurs in a well-defined sequence of six steps. At each step there is a friction response and a height change followed by a stable period (seven stable structures in total). The first point to recognize is that the dissolution is extremely slow compared to the dissolution observed in Figure 1 when the tip impinged at the end of the cancrinite column. The first dissolution event across the middle of the terrace did not occur until 2100 s after over 5000 passes of the tip. This immediately identifies the high stability of the middle of the cancrinite columns relative to their ends.

In order to assess more fully the mechanism of this tip-assisted dissolution the relative energy of the crystal has been modeled as tetrahedral silicate units are removed from the surface. This maps with the surface density of exposed silanol (−SiOH) groups. Low energy surfaces have a highly cross-linked surface with closed-cage structures; high energy surfaces have open cages and a consequent high density of surface silanol groups. Figure 7 shows the energy profile for dissolution of one complete terrace which reveals seven stable, or metastable, structures and six activated transitory structures. Moreover, the height of the seven stable intermediate surfaces correlates with the heights measured by AFM. Each metastable structure exposes only Q_3-type framework species at the surface of the crystal. The stability of the structures, related to the activation energy for the dissolution process, is proportional to the time for which the structure is stable. The complete cancrinite column is the most stable structure and is stable for 2100 s under these conditions. Subsequent depleted cancrinite columns are less stable and dissolve in progressively less time. At each dissolution event there is an associated lateral force or twisting motion imparted to the tip. As the lateral spring constant for the cantilever is known, it is possible to convert this twist into an energy which is imparted to the cantilever over and above the

(31) Kopta, S.; Salmeron, M. *J. Chem. Phys.* **2000**, *113*, 8249–8252.
(32) Trinh, T. T.; Jansen, A. P. J.; van Santen, R. A.; Meijer, E. J. *J. Phys. Chem. C* **2009**, *113*, 2647–2652.
(33) Trinh, T. T.; Jansen, A. P. J.; van Santen, R. A. *J. Phys. Chem. B* **2006**, *110*, 23099–23106.
(34) Cotton, A. *Biosci. Horizons* **2008**, *1*, 38–43.
(35) See Supporting Information.
(36) Brady, P. V.; Walther, J. V. *Geochim. Cosmochim. Acta* **1989**, *53*, 2823–2830.

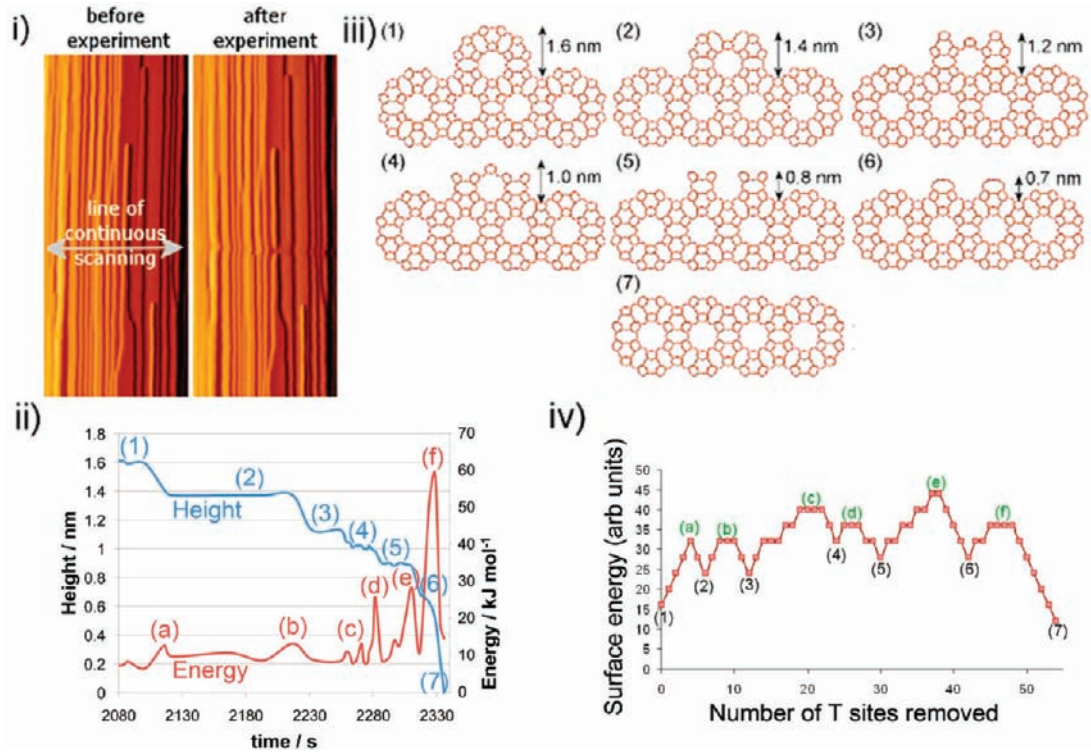

Figure 7. Stepwise unstitching of the zeolite L structure. Observations from continuously scanning the AFM tip over a bridging cancrinite array where (i) shows the vertical deflection micrographs obtained before and after the experiment; it can be seen that after the experiment the terrace has been cut in the position where scanning took place. The graph in (ii) shows the height and friction measured at a particular time; the friction increased when the height decreased in a series of steps (friction is recorded as the energy stored in the cantilever twist). For example (a) in the friction graph corresponds to the removal of units between positions (1) and (2) in the height graph. The schematic in (iii) shows seven different structures corresponding to the heights of stable structures observed. The graph in (iv) was simulated using a procedure similar to that described in Chiu et al.[19] and represents the relative stability of units based upon the number of hydroxyl groups exposed to the surface. Sites marked (a)−(f) are unstable conformations, whereas (1)−(7) are relatively more stable and correspond to closed-cage configurations. The stable sites are in excellent correspondence to the heights observed on the AFM time scale. Similarly, the unstable sites correspond to an increase in friction in the experiment. The stability of the sites is also related to the time before they dissolve. For example, the most stable surface (1) persists for 2100 s whereas the less stable site (4) only persists for 30 s.

background cantilever twist.[35] This energy may be the result of a number of processes including the enthalpy of bond breakage and energy transfer into heating processes. Also, as the tip penetrates deeper into the terrace, more and more of the terrace will be removed both laterally as well as normal to the surface, depending on the tip profile. Nevertheless, it is possible with a known tip size to estimate the number of bonds that will be broken during the dissolution. As the tip has a radius of *ca.* 40 nm, the minimum number of bonds that will be broken to cut the entire 1.6 nm terrace will be *ca.* 190 in steps of between 10 and 60 bonds. If all the bonds in the zeolite are broken (which is not required for structural removal), the total number would increase to about 550 bonds. An investigation carried out by Navrotsky measured the enthalpy of formation of an aluminosilicate dimer (TO_2) of FAU using calorimetry, giving a value of −2.38 kJ mol^{-1}.[37] By making the zeroth-order assumption that the enthalpy for dissolution is the reverse process (+2.38 kJ mol^{-1}) it is not unreasonable to expect about 20−100 kJ mol^{-1} to be associated with each dissolution step as observed. This unstitching approach is somewhat akin to the unfolding of proteins *via* extraction with an AFM cantilever while monitoring the stepwise force.[38] In this case, however, the crystal is dissolved stepwise through a tip-aided process and the energetics recorded through lateral deflection forces.

3.3. Monte Carlo Simulations. That the crystal dissolves stepwise *via* intermediate closed-cage structures is a very significant result that helps enormously to model crystal growth and dissolution processes in framework materials in general. It establishes experimentally, for the first time, that closed-cage structures are significantly more stable than open structures. This allows a decoupling of the time scale of molecular events from the time scale of persistence of larger cage structures. Therefore, it is valid to model the crystal growth through a coarse-grain description of cage structures (the rate-determining entities) even though the crystal probably grows *via* much smaller units such as monomers or small oligomers. This makes an enormously complicated task much more tractable. The principle of these techniques should be more widely applicable to the study of crystal modifications in general.

The basic mechanism of both growth and dissolution is revealed by these AFM and HRSEM images (dissolution directly from the *in situ* AFM measurements and growth from Monte Carlo calculations, Figure 8, of the surface topology of quenched crystals).

In order to model the growth of zeolite L the structure was first coarse grained into closed cages that are known to be stable, both from structure calculations and also from the experimental evidence from the AFM dissolution on a single line scan. This shows the cancrinite cage to be the most stable unit and can therefore be considered as the rate-determining unit. It is important to stress that this does not suggest that the cancrinite cage is the fundamental growth unit, which

(37) Yang, S.; Navrotsky, A.; Phillips, B. L. *Microporous Mesoporous Mater.* **2001**, *46*, 137–151.

(38) Best, R. B.; Brockwell, D. J.; Toca-Herrera, J. L.; Blake, A. W.; Smith, D. A.; Radford, S. E.; Clarke, J. *Anal. Chim. Acta* **2003**, *479*, 87–105.

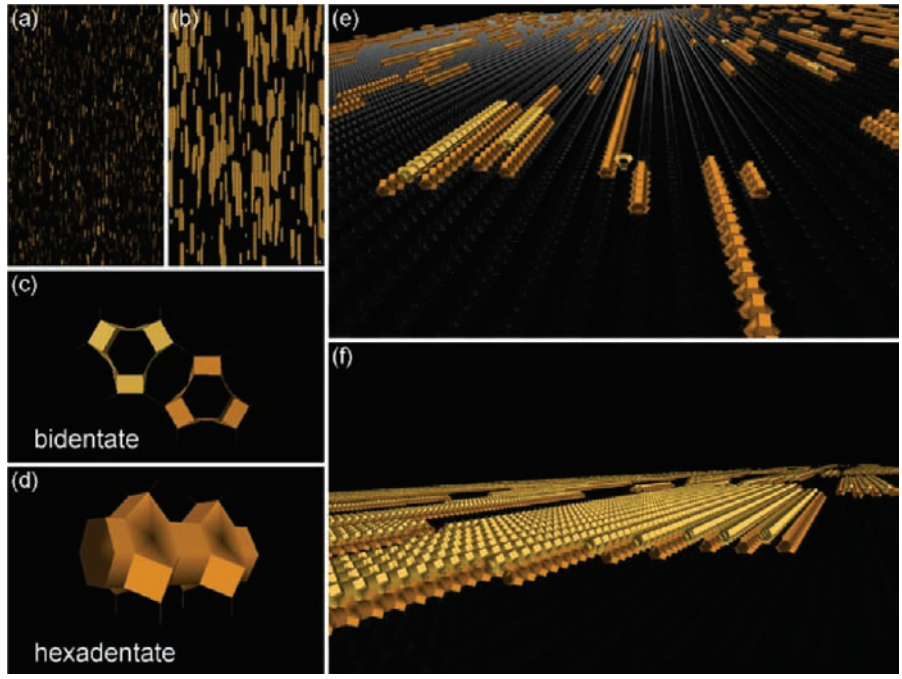

Figure 8. Monte Carlo simulation of the surface crystal growth on zeolite L. For an internal energy stabilization of a bidentate linkage, U_B, of 4 kcal mol^{-1}. (a) and (b) show a 2-dimensional simulation for the situation at high supersaturation and equilibrium. The calculations were performed considering the two cancrinite cage linkages shown in (c) and (d). A bidentate linkage with stabilization energy U_B and a hexadentate linkage with stabilization energy U_H. (e) and (f) show close up images of simulations (a) and (b) respectively. Under supersaturated conditions (e) growth is dominated by a high nucleation density of single cancrinite columns that form pillars and bridge when adjacent. Some terrace spreading *via* unfavorable $L_{1,0}$ linkages is also apparent (compare with Figure 2). Near to equilibrium (f) 2-dimensional Ostwald ripening reduces the concentration of remaining individual cancrinite columns and terraces, elongated in the *c*-direction with curved shoulders are prevalent.

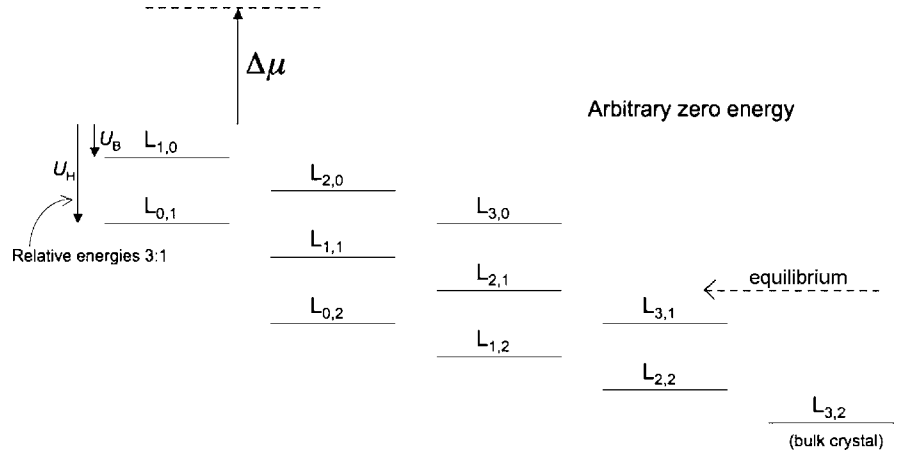

Figure 9. Schematic diagram relative energy scale for different linkages of cancrinite cages in zeolite L. The linkage nomenclature $L_{m,n}$ signifies *m* bidentate linkages and *n* hexadentate linkages. Each bidentate linkage is stabilized by an internal energy U_B and each hexadentate linkage by an internal energy U_H ($U_H = 3U_B$). The driving force, $\Delta\mu$, can either be kept fixed in the Monte Carlo program or be allowed to drop to achieve equilibrium when the growth and dissolution rates are equal. The unknown internal energies U_B and U_H are determined by simulating the growth features of zeolite L observed by AFM. The driving force for crystallization, $\Delta\mu$, decreases for a growth event and increases for a dissolution event that permits the equilibrium position for the driving force to be established. This lies close to energy level $L_{2,1}$, independent of the value of U_B.

may be much smaller, even a monomer. Cancrinite cages are connected *via* two motifs in zeolite L. A side attachment consists of a bidentate Si−O−Si linkage and a cancrinite column attachment that consists of a hexadentate Si−O−Si linkage. A fully coordinated cancrinite cage is bound by three bidentate and two hexadentate linkages (this is termed $L_{3,2}$). Fresh nucleation on a $\{10\bar{1}0\}$ surface is governed by a $L_{1,0}$ linkage, growth of a cancrinite column in the *c*-direction is governed by a $L_{1,1}$ linkage and growth of a cancrinite cage orthogonal to the *c*-direction is initiated by a $L_{1,0}$ linkage (the same as surface nucleation). It is not unreasonable to assume that the hexadentate linkage is stabilized three times as much as a bidentate linkage. Consequently, all the possible surface structures can be placed on an energy scale as shown in Figure 9. For a thermodynamically reversible process the ratio of the probability for growth to the probability of dissolution for each site with linkage $L_{m,n}$, $P_G^{L_{m,n}}/P_D^{L_{m,n}}$, is given by[39]

$$\frac{P_G^{L_{m,n}}}{P_D^{L_{m,n}}} = \exp\left(\frac{(mU_B + nU_H)}{kT} + \frac{\Delta\mu}{kT}\right) \qquad (6)$$

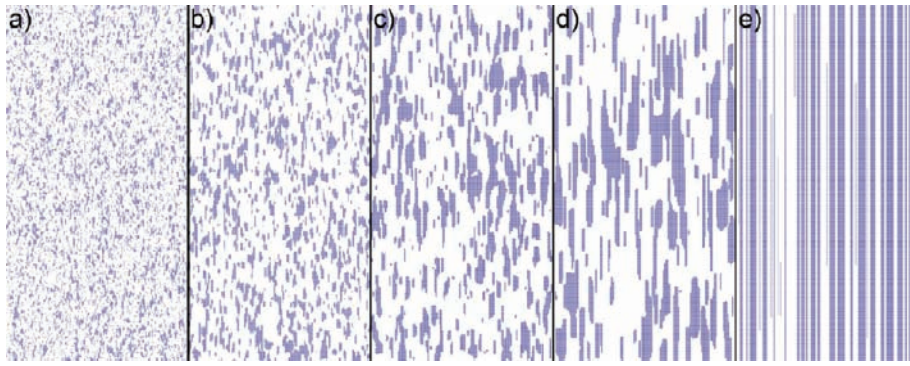

Figure 10. Monte Carlo calculations of the surface of zeolite L at equilibrium. The simulations have been performed at 180 °C with a stabilization of the bidentate attachment U_B of (a) 1 kcal mol^{-1}; (b) 2 kcal mol^{-1}; (c) 3 kcal mol^{-1}; (d) 4 kcal mol^{-1}; (e) 8 kcal mol^{-1}. Each panel represents a section 0.29 μm by 0.49 μm.

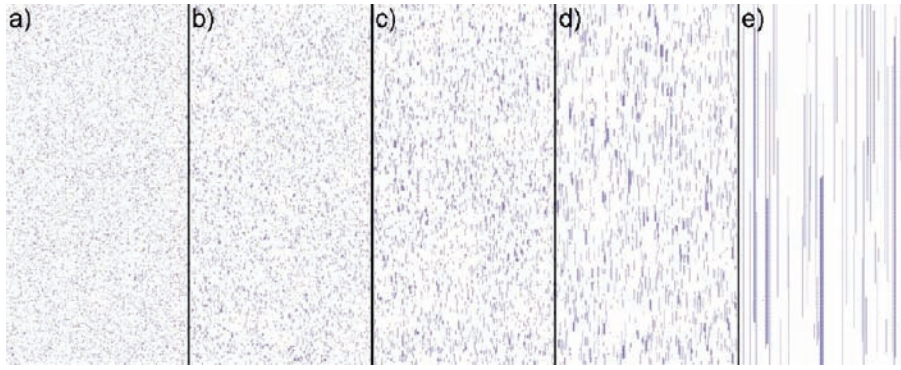

Figure 11. Monte Carlo calculations of the surface of zeolite L at high supersaturation. The simulations have been performed at 180 °C with a stabilization of the bidentate attachment U_B of (a) 1 kcal mol^{-1}; (b) 2 kcal mol^{-1}; (c) 3 kcal mol^{-1}; (d) 4 kcal mol^{-1}; (e) 8 kcal mol^{-1}. Each panel represents a section 0.29 μm by 0.49 μm.

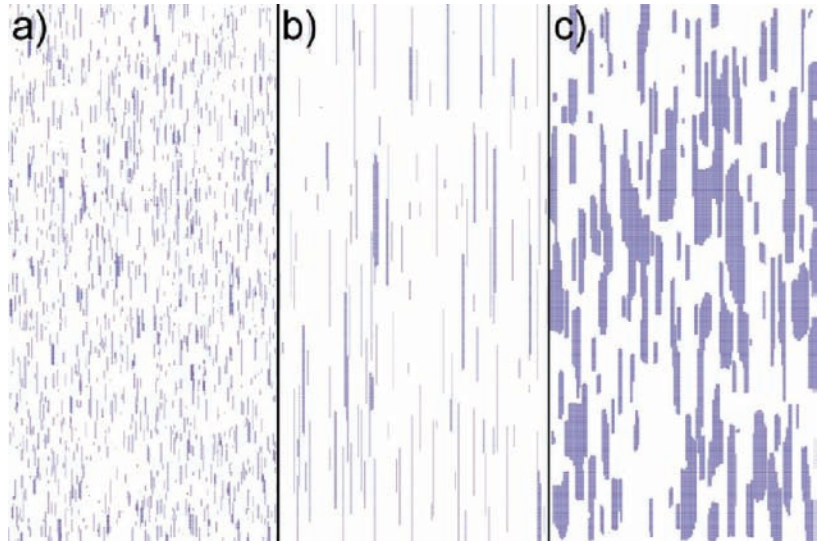

Figure 12. Monte Carlo calculations of the surface of zeolite L at $U_B = 4$ kcal mol^{-1}. The simulations have been performed at 180 °C using different driving force or supersaturation: (a) high-supersaturation ($\Delta\mu$ above $L_{1,0}$); (b) low-supersaturation ($\Delta\mu$ between $L_{0,1}$ and $L_{1,1}$); (c) equilibrium saturation. Each panel represents a section 0.29 μm by 0.49 μm.

where m and n are the number of bidentate and hexadentate linkages respectively, $\Delta\mu$ is the driving force (related to the supersaturation) and U is the internal energy. If we make the assumption that the internal energy stabilization of the hexadentate linkage, U_H, is three times that of the bidentate linkage, U_B, then the simulation need only be optimized for one internal energy at a given supersaturation. Absolute probabilities for growth and dissolution assuming little kinetic influence are given by[39]

$$P_G^{L_{m,n}} = \exp\left(\frac{0.5(mU_B + nU_H)}{kT} + \frac{0.5\Delta\mu}{kT}\right) \qquad (7)$$

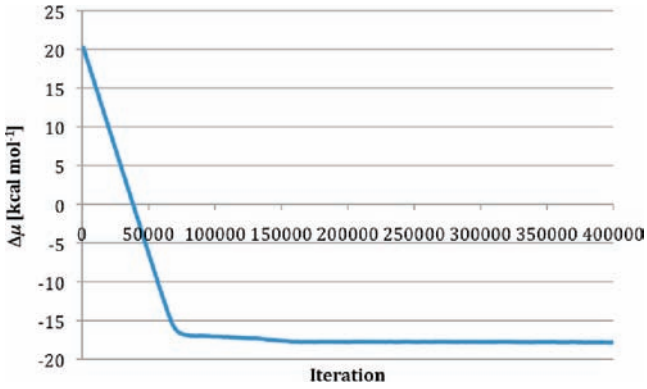

Figure 13. Monte Carlo determination of the equilbrium value of the driving force at 180 °C and $U_B = 4$ kcal mol^{-1}. After *ca.* 60,000 iterations the value of $\Delta\mu$ is nearly constant; however, there is further 2-D Ostwald ripening until *ca.* 180,000 iterations. The final equilibrium point is just above $L_{2,1}$.

and

$$P_D^{L_{m,n}} = \exp\left(\frac{-0.5(mU_B + nU_H)}{kT} - \frac{0.5\Delta\mu}{kT}\right) \qquad (8)$$

A further advantage of the Monte Carlo approach to the problem is that equilibrium is easily established by allowing the driving force, $\Delta\mu$, to drop for a growth event and increase for a dissolution event. Equilibrium is achieved when the number of grown sites remains constant and the overall growth features remain equivalent (all Ostwald ripening has occurred). In this manner the position of $\Delta\mu$ relative to the crystal surface energy levels at equilibrium is also established. This is equivalent to the center of gravity of the energy levels coupled with the number of each kind of surface site. Figures 10−12 show a range of calculations with different internal energy values and driving force. It is readily established that a good fit with experimental data is achieved near to $U_B = 4$ kcal mol^{-1}. At $U_B = 1.0$ kcal mol^{-1} there is not enough distinction between growth in the *c* and *a* directions. Above $U_B = 4.0$ kcal mol^{-1} the terraces are much more rectilinear than observed and there is little stabilization of single cancrinite columns near equilibrium as observed experimentally. The equilibrium driving force is established (Figure 13) by driving the simulation to, first, a constant number of growth units and, second, complete 2-D Ostwald ripening. The equilibrium driving force is found to lie just above $L_{2,1}$ more or less independent of the value of U_B. Further, corroboration of the stabilization energies comes from the three-dimensional Monte Carlo simulation (Figure 14) which provides a determination of the aspect ratio of the crystal as well as the terrace structure. The experimental crystal aspect ratio, *c*/*a*, is *ca.* 4 and, as can be seen from Table 2, this is replicated at a value U_B equal to *ca.* 2.5 kcal mol^{-1}, not too dissimilar to the value of 4.0 kcal mol^{-1} determined from terrace structure. Zeolite L is notorious for the incorporation of internal defects that result in a foreshortening of the *c*-length of the crystal; indeed most low aspect ratio crystals have a large number of such defects. This may account for the shortening of the *c*-length of the crystals that, in this case, are predicted to have an aspect ratio of *ca.* 10 at U_B equal to 4.0 kcal mol^{-1}.

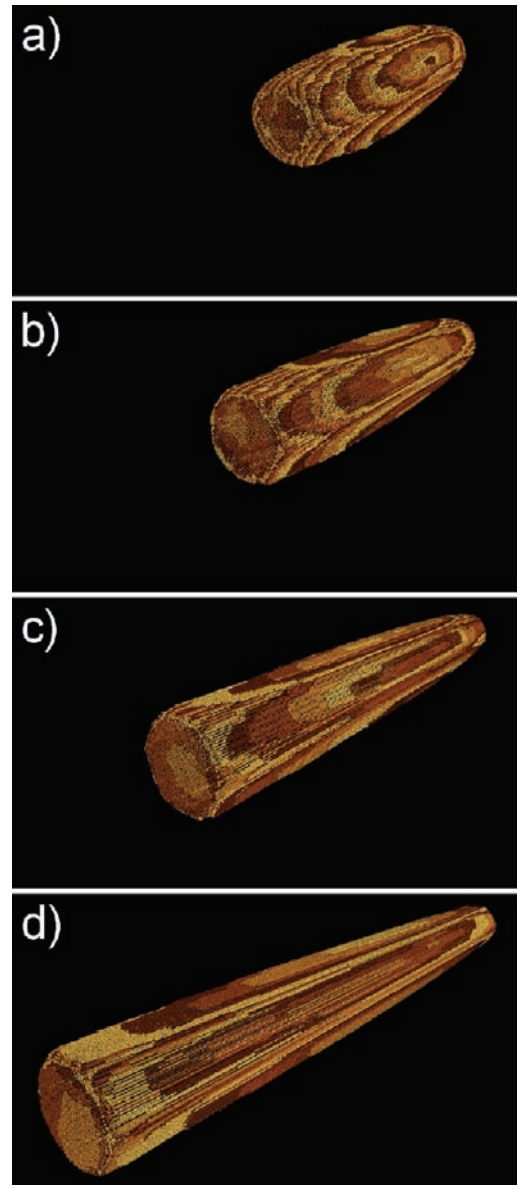

Figure 14. Three-dimensional Monte Carlo simulation of LTL showing change in aspect ratio for different values of the energy stabilization for bidentate attachement: (a) $U_B = 2.5$ kcal mol^{-1}; (b) $U_B = 3.0$ kcal mol^{-1}; (c) $U_B = 3.5$ kcal mol^{-1}; (d) $U_B = 4.0$ kcal mol^{-1}.

Table 2. Aspect Ratio of LTL Crystal from 3-Dimensional Monte Carlo Simulation as Function of Energy of Bidentate Attachment of Cancrinite Cage

energy U_B (kcal/mol)	aspect ratio (*c*/*a*)
0.0	1.0
0.5	1.3
1.0	1.6
1.5	2.2
2.0	3.1
2.5	4.5
3.0	6.4
3.5	8.4
4.0	10.8
4.5	15
7.0	65

The preponderance of long cancrinite columns, most clearly seen in the HRSEM images, combined with the rapid dissolution of these features revealed by AFM shows that terrace dissolution

(39) Boerrigter, S. X. M.; Josten, G. P. H.; van de Streek, J.; Hollander, F. F. A.; Los, J.; Cuppen, H. M.; Bennema, P.; Meekes, H. *J. Phys. Chem. A* **2004**, *108*, 5894–5902.

in the *c*-direction on this facet is orders of magnitude greater than terrace dissolution in the orthogonal *a*-direction. This is further corroborated by the prevalence of shoulders that are created as two adjacent terraces merge by a column capping the large 12-ring structure (see Figure 2 and Figure 8). Terrace spreading orthogonal to the *c*-direction is controlled by the same energetics for fresh nucleation on a $\{10\bar{1}0\}$ facet. That is, it is an unfavorable event initiated *via* completion of a single cancrinite cage through a bidentate link (linkage $L_{1,0}$ in Figure 8). As a consequence dissolution of such a structure before the terrace propagates further, and therefore sticks, is highly likely. Growth in the column direction is governed by completion of hexadentate linkages that will be three times more stable. This is borne out by Monte Carlo growth calculations that reveal the cancrinite cages are stabilized by about 2 kcal mol^{-1} for each linkage to the growing crystal. With such a stabilization energy many of the growth features of the crystal are replicated: single cancrinite columns are stabilized; terraces have a high *c*/*a* direction aspect ratio; shoulders are observed where terraces merge; terrace spreading orthogonal to the cancrinite column direction is aided by a high nucleation density of single columns which are then bridged. These calculations illustrate an important problem in the effort to crystallize large pore nanoporous materials. Circumventing the large pore, in this case a 12-ring channel, requires a multistep process and consequently, at best, will be seriously retarded without the addition of organic templating molecules to act as a scaffold. Conversely, this also illustrates how a crystal, in the absence of an organic templating agent, can overcome this significant obstacle by first laying down pillars that are subsequently bridged (see Figure 2).

Finally, our work covers two temperature regimes: *in situ* dissolution measurements made at or just above room temperature from which an activation energy has been extracted; *ex situ* measurements on crystals grown at 180 °C which form the basis for the Monte Carlo studies and establishment of surface energies of stabilization. Despite the large differences in temperature in the two parts of this work the picture that emerges is consistent. Rapid dissolution at low temperature occurs, and is highlighted in the AFM, at cancrinite column termini and at shoulder sites. This is completely consistent with the sites predicted for rapid growth from the Monte Carlo studies that simulate high temperature experiments. Consequently, this gives weight to the conjecture that the processes occurring in the two temperature regimes are similar with suitably different rates.

4. Conclusions

In conclusion we have established that AFM can be used to target and highlight exactly where the chemistry is taking place during *in situ* crystal transformations. This leads directly to the activation energy for specific nanoscopic processes at the crystal surface. Then by utilizing a tip-aided dissolution process it is possible to unstitch the crystal, unit by unit, thereby discerning the relative stability of the different crystal surfaces. These results also establish that a coarse-grained approach to Monte Carlo simulation of crystal growth processes is valid for nanoporous systems and obviates the need to consider growth in terms of monomers or small oligomers. This allows a determination of the stabilization energies of cage structures at the growing surface necessary in order to understand how to control properties such as crystal habit.

Acknowledgment. The authors would like to acknowledge EPSRC, ExxonMobil Research and Engineering and The Knut and Alice Wallenberg Foundation for financial support.

Supporting Information Available: The method for determination of lateral force constants, forces, and energies; determination of tip shape; associated AFM observations of nanoporous zincophosphates. This material is available free of charge via the Internet at http://pubs.acs.org.

JA105593V